



# Innovation-based Kalman filter fault detection and exclusion method against all-source faults for tightly coupled GNSS/INS/Vision integration

Haitao Jiang<sup>1</sup> · Dayu Yan<sup>1</sup> · Jiale Wang<sup>1</sup> · Jie Yin<sup>2</sup>

Received: 18 May 2023 / Accepted: 22 January 2024 / Published online: 23 April 2024  
© The Author(s), under exclusive licence to Springer-Verlag GmbH Germany, part of Springer Nature 2024

## Abstract

Safety-critical navigation systems often involve multiple sensor types, including global navigation satellite system (GNSS), to enhance positioning accuracy. Additionally, the systems' reliability has been significantly improved through the application of fault detection and exclusion (FDE) techniques. An enhanced AIME (Autonomous Integrity Monitoring by Extrapolation) method is introduced in our approach to identify faulty satellites. This is accomplished by analyzing the measured Kalman filter (KF) innovations and their covariances within a sliding window. Furthermore, a strategy for fault separation, detection, and exclusion is developed for GNSS and IMU, making use of their relationship within the KF innovation vector derived from the GNSS measurement model. Similarly, the innovation vector derived from the visual measurement model is employed to detect visual faults, with the assumption that the inertial measuring unit (IMU) is fault-free. Upon detecting faults, we proceed to redesign the system noise matrix and measurement noise matrix within the KF using test statistics, effectively excluding measurement faults from satellites and IMU. In order to assess the performance of our proposed method, we conducted a field test utilizing the collected vehicle-mounted dataset. The results demonstrate the effectiveness of our FDE method in accurately identifying faulty satellites, detecting IMU faults of varying magnitudes, and excluding abnormal visual observations. Furthermore, after fault exclusion, the maximum position error during the fault time period decreased by an average of 62%.

**Keywords** GNSS/INS/Vision integration · Kalman filter · Sensor faults · Enhanced AIME · Fault detection and exclusion

## Introduction

Accurate and reliable navigation information is essential in safety-critical applications, including autonomous driving, service robotics (Yin et al. 2021), and unmanned aerial vehicles (UAVs) (Groves 2013; Wang et al. 2020). To improve the positioning accuracy of the system in intricate environments, integration of global navigation satellite system (GNSS) with inertial navigation systems (INS) and visual navigation systems is a common practice. This integration is preferred due to their complementary characteristics

(Backén et al. 2012; Cao et al. 2021; Groves 2013; Li et al. 2019). Furthermore, the extended Kalman filtering (EKF) algorithm, known for its optimal estimation capabilities, finds extensive use in the fusion of multi-sensor data. Concurrently, there has been growing interest in fault detection and exclusion (FDE) techniques for multi-sensor integrated navigation systems, which protect users from the risk of potential sensor faults.

The occurrence of sensor faults in integrated navigation systems is a critical issue, that not only affects navigation performance but is also closely related to safety. In the system, typically two types of faults are encountered: step errors and slow-growing errors (SGEs). SGEs, which are common faults in pseudorange measurements, pose a particular challenge in terms of detection (Bhatti et al. 2007). This difficulty arises because SGEs exhibit gradual growth over time, leading to a gradual degradation in the accuracy of estimated states without early detection. Several FDE methods have been explored for tightly coupled GNSS/INS integration in

✉ Haitao Jiang  
by1902019@buaa.edu.cn

<sup>1</sup> School of Electronic Information Engineering, Beihang University, 37 Xueyuan Road, Beijing 100083, China

<sup>2</sup> Institute for Sensing and Navigation, Shanghai Jiao Tong University, 800 Dongchuan Road, Shanghai 200240, China

recent years. These methods can be classified as observation-domain or position-domain methods, depending on whether the fault detection (FD) method is derived from measurements or position solutions (Jing et al. 2022). In the case of observation-domain methods, typical approaches include AIME (Autonomous Integrity Monitoring by Extrapolation) (Diesel and Luu 1995) and CRAIM (Ochieng and Feng 2008) methods. These methods utilize use the vector of measurement residuals within the filter algorithm (KF or EKF) to calculate the test statistic. Many other algorithms have been developed based on this foundation. For instance, Yang (2014) introduced an improved MEMS-INS/GNSS integrated system with fault detection and exclusion capabilities for land vehicle navigation in urban areas, while the rate detector (RD) algorithm was proposed by (Bhatti et al. 2012). These algorithms are specifically designed to enhance the system's positioning performance during GNSS data disturbances and improve the capacity for detecting SGEs, respectively. Among the position-domain methods, multiple solution separation (MSS) (Brenner 1996), multiple hypothesis solution separation (MHSS) (Tanil et al. 2019), and advanced RAIM (ARAIM) (Blanch et al. 2007, 2018; Pan et al. 2019) are the most representative FDE algorithms. The test statistic in these methods is computed by comparing the full set solution with subset solutions. However, it should be noted that these methods can be computationally intensive in certain situations. The FD methods can also be divided into "snap-spot" and "sequential" algorithms according to whether they are derived from current information or historical information. In the above-mentioned methods, AIME is a "sequential" algorithm, while MSS is a "snap-spot" algorithm.

The methods mentioned above primarily concentrate on GNSS faults, with limited attention given to IMU faults. Nonetheless, it is worth noting that IMU can also produce faulty measurements, particularly in the case of MEMS IMU (Pasquale and Soma 2010). These faulty IMU measurements can have a severe worse impact on the system, potentially leading to critical incidents in various domains, including civil aviation accidents (Crispoltoni et al. 2018). In the context of vehicle navigation, where cost-effective IMUs are often utilized, the significance of addressing IMU faults cannot be overstated. IMU FDE is indispensable to ensure the reliability and safety of the navigation system. Recently, Lee and Liu et al. (Lee et al. 2018; Liu et al. 2019) conducted an integrity monitoring scheme tailored for UAVs to handle IMU faults. However, it is important to note that these methods primarily focus on deriving position error overbounding rather than IMU FDE. On the other hand, Wang et al. (2020) presented a two-step FDE approach designed to detect both GNSS and IMU faults within a system. Simulation experiments conducted on aircraft have demonstrated the effectiveness of this method. However, these methods cannot

quickly detect faulty satellites, and there is no simple and effective fault exclusion strategy; this approach still has a serious impact on the positioning performance of the system when IMU faults occur. In addition, when the satellite signal is blocked, the positioning performance and fault detection performance of the system both significantly deteriorate.

To ensure accurate and safety-assured navigation solutions for vehicle systems, we present an effective FDE method that includes all-source faults through tightly coupled GNSS/INS/Vision integration. Initially, a sliding window of size  $l$  is established, and the innovation vector of the EKF is categorized based on satellite numbers. Subsequently, following the approach described in (Wang et al. 2020), we employ a two-step FDE method to identify fault sources. In the third step, fault exclusion strategies are devised to mitigate the impact of faulty measurements on the estimated system state. To assess the performance of our proposed method, we conduct a thorough analysis of the detection capabilities of AIME and our method. Additionally, we evaluate the positioning accuracy of the system both before and after the implementation of the FDE schemes.

Our paper begins by introducing the tightly coupled GNSS/INS/Vision integration with FDE, including the system architecture, the GNSS/INS/Vision integration model, and a comprehensive analysis of fault sources. This is followed by an intricate explanation of the fault detection and exclusion methodologies. We then analyze field test results to measure the effectiveness of the proposed method. Finally, the conclusions are presented.

### Tightly coupled GNSS/INS/Vision integration with fault detection and exclusion

This section first introduces the coordinate frames (Cao et al. 2021). Subsequently, we detail the architecture of the tightly coupled GNSS/INS/Vision integration, which includes fault detection and exclusion mechanisms. Following that, we provide a comprehensive description of the tightly coupled GNSS/INS/Vision integration model. Lastly, we elucidate the sources of faults within the system.

#### Architecture of tightly coupled GNSS/INS/Vision integration with fault detection and exclusion

The system's architecture is visually represented in Fig. 1. The system is segmented into four distinct components: INS mechanization, GNSS measurement modeling, visual measurement modeling, and fault detection and exclusion. The initial component, INS mechanization, utilizes raw IMU data to generate navigation solutions, including position, velocity, and attitude. Moving to the second part, GNSS measurement modeling, the difference between GNSS pseudorange and pseudorange rate measurements, and the pseudorange

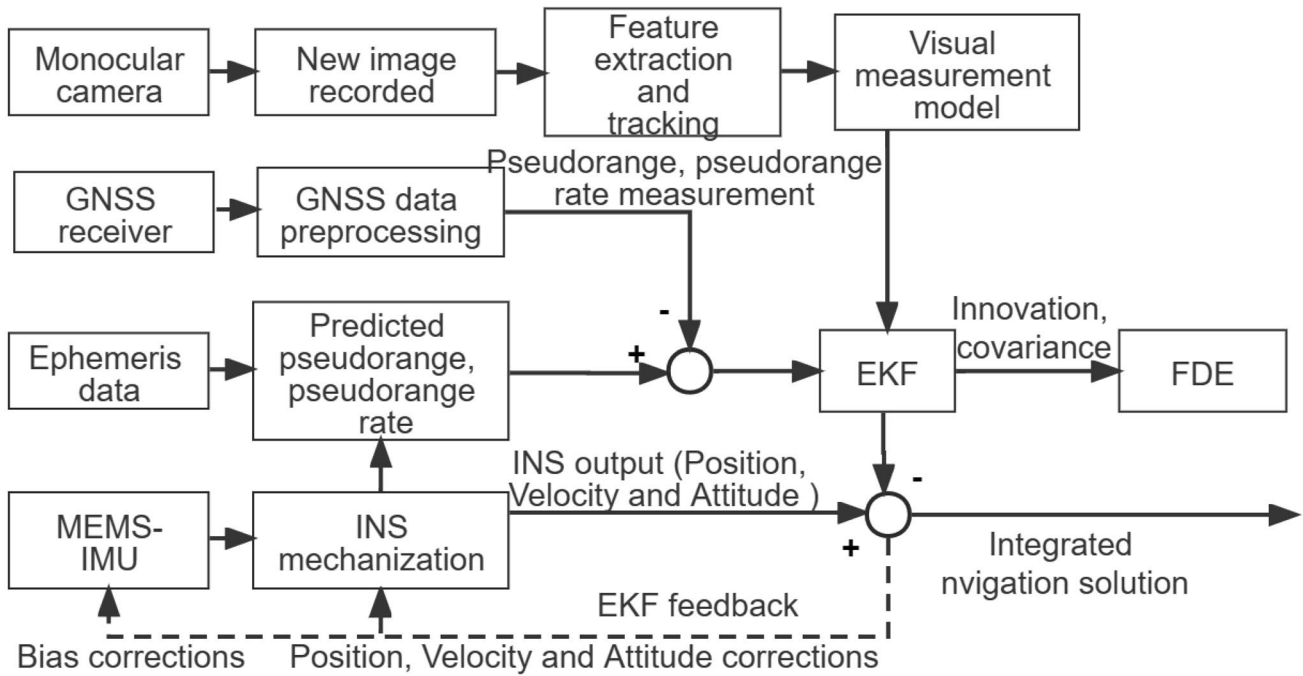


**Fig. 1** Architecture of the tightly coupled GNSS/INS/Vision integration with fault detection and exclusion. *EKF* extended Kalman filtering, *FDE* fault detection and exclusion), *GNSS* global navigation satellite system, *IMU* inertial measuring unit, and *INS* Inertial navigation system

and pseudorange rate predicted by the INS are employed as measurement vectors. These vectors are utilized to update the states of the EKF, following the approach outlined in (Chen et al. 2021). The third component involves visual measurement modeling, and the integration of vision and INS is executed using the classic MSCKF model (Mourikis and Roumeliotis 2007). When a new image is received, the error state and covariance of the current IMU pose are incorporated into the EKF. Additionally, the extraction and tracking of features are carried out. This method employs the reprojection errors of feature points as measurement vectors for updating the system’s state. Following the EKF update, the estimated state error vector is utilized to correct the navigation solutions produced by the INS and adjust the IMU bias. The final component, fault detection and exclusion, is geared toward preventing inaccurate state estimation results from adversely affecting the system’s performance. The innovation vector and covariance matrix of the EKF are used to calculate the test statistic, which is compared with the corresponding test threshold to assess whether the sensor measurements are faulty.

**Tightly coupled GNSS/INS/Vision integration model**

Based on the various combinations of sensors utilized, this system can be categorized into two segments: tightly coupled GNSS/INS integration and Vision/INS integration. These segments are interconnected through the IMU poses. The INS

dynamic model is formulated within the earth-centered earth-fixed (ECEF) frame, and the bias error of the IMU is represented as a first-order Gauss–Markov process. The error state vector of the system at epoch *k* can be expressed as follows:

$$\delta x_k = \left[ (\delta x_{I,k})^T (\delta x_{G,k})^T (\delta \theta_{C,ki})^T (\delta p_{C,ki}^e)^T \right]^T \tag{1}$$

Then,  $\delta x_{I,k}$  and  $x_{G,k}$  are expressed as:

$$\begin{cases} \delta x_{I,k} = \left[ (\delta p_{I,k}^e)^T (\delta v_{I,k}^e)^T (\delta \phi_{I,k}^e)^T (b_g)^T (b_a)^T \right]^T \\ \delta x_{G,k} = [\delta b_r \ \delta d_r]^T \end{cases} \tag{2}$$

where  $\delta p_{I,k}^e$ ,  $\delta v_{I,k}^e$ , and  $\delta \phi_{I,k}^e$  are the position, velocity, and attitude error vectors of the IMU in the *e*-frame, respectively;  $b_g$  and  $b_a$  are the bias errors of the gyroscope and accelerometer, respectively; and  $\delta b_r$  and  $\delta d_r$  are receiver clock bias and its drift.  $\delta \theta_{C,ki}$  and  $\delta p_{C,ki}^e$  ( $i = 1 \dots M$ ) are the attitude and position error vectors corresponding to the *i*-th IMU fixed to the camera; *M* denotes the total number of poses in the sliding window. In the IMU frame, the accelerometer  $\tilde{f}^b$  and gyroscope  $\tilde{w}_{ib}^b$  can be measured as follows:

$$\begin{cases} \tilde{f}^b = f^b + b_a + w_a \\ \tilde{w}_{ib}^b = w_{ib}^b + b_g + w_g \end{cases} \tag{3}$$

where  $f^b$  and  $w_{ib}^b$  represent the noise-free measurements of the accelerometer and gyroscope, respectively;  $w_a$  and  $w_g$  represent the random noise of the gyroscope and accelerometer, respectively.

**GNSS measurement model**

The measurement vector comprises two components: the pseudorange measurement vector and the pseudorange rate measurement vector. In the discrete-time domain, it can be represented as follows:

$$\begin{aligned} \begin{bmatrix} \rho_I - \rho_G \\ \dot{\rho}_I - \dot{\rho}_G \end{bmatrix} &= \begin{bmatrix} \mathbf{H}_{k,\rho} \\ \mathbf{H}_{k,\dot{\rho}} \end{bmatrix} \begin{bmatrix} \delta \mathbf{x}_{I,k} \\ \delta \mathbf{x}_{G,k} \end{bmatrix} + \boldsymbol{\varepsilon}_{\text{GL},k} \\ &= \mathbf{H}_{\text{GL},k} \begin{bmatrix} \delta \mathbf{x}_{I,k} \\ \delta \mathbf{x}_{G,k} \end{bmatrix} + \boldsymbol{\varepsilon}_{\text{GL},k} \end{aligned} \tag{4}$$

where  $\rho_G$  and  $\dot{\rho}_G$  represent the pseudorange and pseudorange rate vectors of GNSS measurements, respectively;  $\rho_I$  and  $\dot{\rho}_I$  represent the pseudorange and pseudorange rate vectors, respectively, predicted by INS;  $\mathbf{H}_{\text{GL},k}$  denotes the measurement matrix; and  $\boldsymbol{\varepsilon}_{\text{GL},k}$  represents the measurement noise vector, which is modeled as zero-mean Gaussian White Noise (GWN) with covariance matrix  $\mathbf{R}_{\text{GL},k}$ .

For pseudorange measurements, after correcting all the errors except for receiver errors (noise and clock bias), the pseudorange for the  $m$ -th satellite can be modeled as Misra and Enge (2001):

$$\tilde{\rho}_m = \rho_m + c\delta t_r + \varepsilon_m \tag{5}$$

where  $\tilde{\rho}_m$  denotes the measured pseudorange from the  $m$ -th satellite to the receiver;  $c$  denotes the speed of light;  $\delta t_r$  denotes the receiver’s clock offset;  $\varepsilon_m$  denotes the total effect of residual errors; and  $\rho_m$  denotes the actual distance between the receiver and satellite, which can be written as follows:

$$\rho_m = \| \mathbf{x} - \mathbf{x}^m \| = \sqrt{(x - x^m)^2 + (y - y^m)^2 + (z - z^m)^2} \tag{6}$$

where  $\mathbf{x} = [x \ y \ z]^T$  and  $\mathbf{x}^m = [x^m \ y^m \ z^m]^T$  represent the actual receiver position and the  $m$ -th satellite position in the  $e$ -frame, respectively. The corresponding pseudorange of the INS mechanization output can be expressed as follows:

$$\rho_I^m = \sqrt{(x^I - x^m)^2 + (y^I - y^m)^2 + (z^I - z^m)^2} \tag{7}$$

where  $\mathbf{x}^I = [x^I \ y^I \ z^I]^T$  is the position of the INS mechanization output in the  $e$ -frame.

In order to satisfy the fundamental assumptions of the EKF, it is necessary to linearize the measurement equation. Then, the difference between the result of the first-order

Taylor expansion of  $\rho_I^m$  around  $\mathbf{x}$  and  $\tilde{\rho}_m$  can be presented as follows:

$$\begin{aligned} \delta \rho_m = \rho_I^m - \tilde{\rho}_m &\approx e_{m,x} \delta x + e_{m,y} \delta y + e_{m,z} \delta z \\ &\quad - \delta b_r + \varepsilon_m \end{aligned} \tag{8}$$

where  $e_{m,x} = \frac{x - x^m}{\| \mathbf{x} - \mathbf{x}^m \|}$ ,  $e_{m,y} = \frac{y - y^m}{\| \mathbf{y} - \mathbf{y}^m \|}$ ,  $e_{m,z} = \frac{z - z^m}{\| \mathbf{z} - \mathbf{z}^m \|}$ ;  $\delta b_r = c\delta t_r$ ;  $\delta \mathbf{x} = [\delta x \ \delta y \ \delta z]^T$  is the estimated position error. For  $N_{\text{sat}}$  visible satellites, Eq. (8) can be written as follows:

$$\begin{aligned} \rho_I - \rho_G &= \begin{bmatrix} \rho_I^1 - \tilde{\rho}_1 \\ \rho_I^2 - \tilde{\rho}_2 \\ \vdots \\ \rho_I^{N_{\text{sat}}} - \tilde{\rho}_{N_{\text{sat}}} \end{bmatrix} = \mathbf{G}_{N_{\text{sat}} \times 3}^\rho \begin{bmatrix} \delta x \\ \delta y \\ \delta z \end{bmatrix}_{3 \times 1} \\ &\quad - \begin{bmatrix} \delta b_r \\ \delta b_r \\ \vdots \\ \delta b_r \end{bmatrix}_{N_{\text{sat}} \times 1} + \begin{bmatrix} \varepsilon_1 \\ \varepsilon_2 \\ \vdots \\ \varepsilon_N \end{bmatrix}_{N_{\text{sat}} \times 1} \end{aligned} \tag{9}$$

And  $\mathbf{G}_{N_{\text{sat}} \times 3}^\rho$  can be expressed as follows:

$$\mathbf{G}_{N_{\text{sat}} \times 3}^\rho = \begin{bmatrix} e_{1,x} & e_{1,y} & e_{1,z} \\ e_{2,x} & e_{2,y} & e_{2,z} \\ \vdots & \vdots & \vdots \\ e_{N_{\text{sat}},x} & e_{N_{\text{sat}},y} & e_{N_{\text{sat}},z} \end{bmatrix}_{N_{\text{sat}} \times 3} \tag{10}$$

where  $\rho_I = [\rho_I^1 \ \rho_I^2 \ \dots \ \rho_I^{N_{\text{sat}}}]^T$ ;  $\rho_G = [\tilde{\rho}_1 \ \tilde{\rho}_2 \ \dots \ \tilde{\rho}_{N_{\text{sat}}}]^T$ .

For pseudorange rate measurements, the measured pseudorange rate can be modeled as follows:

$$\begin{aligned} \tilde{\rho}_m &= e_{m,x}(v_x - v_x^m) + e_{m,y}(v_y - v_y^m) \\ &\quad + e_{m,z}(v_z - v_z^m) + \delta d_r + \dot{\varepsilon}_m \end{aligned} \tag{11}$$

where  $\mathbf{v} = [v_x \ v_y \ v_z]^T$  and  $\mathbf{x}^m = [x^m \ y^m \ z^m]^T$  are the velocity of the receiver and  $m$ -th satellite in the  $e$ -frame, respectively. Similarly, the corresponding pseudorange rate of the INS output is expressed as follows:

$$\begin{aligned} \dot{\rho}_I^m &= e_{m,x}(v_{I,x} - v_x^m) + e_{m,y}(v_{I,y} - v_y^m) \\ &\quad + e_{m,z}(v_{I,z} - v_z^m) \end{aligned} \tag{12}$$

where  $\mathbf{v}^I = [v_{I,x} \ v_{I,y} \ v_{I,z}]^T$  is the velocity of the INS mechanization output in the  $e$ -frame. Then, the difference between the INS output pseudorange rate and the GNSS measured pseudorange rate is written as follows:

$$\begin{aligned} \delta \dot{\rho}_m = \dot{\rho}_I^m - \tilde{\rho}_m &= e_{m,x} \delta v_x + e_{m,y} \delta v_y \\ &\quad + e_{m,z} \delta v_z - \delta d_r + \dot{\varepsilon}_m \end{aligned} \tag{13}$$

For  $N_{\text{sat}}$  visible satellites, Eq. (13) can be expressed as follows:

$$\begin{aligned} \dot{\rho}_I - \dot{\rho}_G &= \begin{bmatrix} \dot{\rho}_1^1 - \tilde{\rho}_1 \\ \dot{\rho}_1^2 - \tilde{\rho}_2 \\ \vdots \\ \dot{\rho}_1^{N_{\text{sat}}} - \tilde{\rho}_{N_{\text{sat}}} \end{bmatrix} = \mathbf{G}_{N_{\text{sat}} \times 3}^{\rho} \begin{bmatrix} \delta v_x \\ \delta v_y \\ \delta v_z \end{bmatrix}_{3 \times 1} \\ &\quad - \begin{bmatrix} \delta d_r \\ \delta d_r \\ \vdots \\ \delta d_r \end{bmatrix}_{N_{\text{sat}} \times 1} + \begin{bmatrix} \dot{\epsilon}_1 \\ \dot{\epsilon}_2 \\ \vdots \\ \dot{\epsilon}_{N_{\text{sat}}} \end{bmatrix}_{N_{\text{sat}} \times 1} \end{aligned} \tag{14}$$

According to (4), (9), and (14),  $\mathbf{H}_{\text{GL},k}$  is written as:

$$\mathbf{H}_{\text{GL},k} = \begin{bmatrix} \mathbf{G}_{N \times 3}^{\rho} & \mathbf{0}_{N \times 3} & \mathbf{0}_{N \times 9} & -\mathbf{1}_{N \times 1} & \mathbf{0}_{M \times 1} \\ \mathbf{0}_{N \times 3} & \mathbf{G}_{N \times 3}^{\rho} & \mathbf{0}_{N \times 9} & \mathbf{0}_{M \times 1} & -\mathbf{1}_{N \times 1} \end{bmatrix}_{2N_{\text{sat}} \times 17} \tag{15}$$

where  $\mathbf{0}_{N \times 3}$  denotes a matrix with  $N$  rows and 3 columns and all of its elements are zero;  $\mathbf{1}_{N \times 1}$  denotes a vector with  $N$  rows and 1 column and all of its elements are one.

### Visual measurement model

A single static feature point  $f_j$  is observed by the camera pose  $\mathbf{C}_i$ . The measurement innovation of  $f_j$  on  $\mathbf{C}_i$  can be written as follows:

$$\delta \mathbf{z}_i^{(j)} = \mathbf{z}_i^{(j)} - \hat{\mathbf{z}}_i^{(j)} \tag{16}$$

where  $\mathbf{z}_i^{(j)}$  is the feature position measurements;  $\hat{\mathbf{z}}_i^{(j)}$  is the predicted feature position measurements. Linearizing (16) around  $\delta \mathbf{x}_{I,k}$  and feature position  $\hat{\mathbf{p}}_j^e$  in the e-frame, we can obtain the following:

$$\delta \mathbf{z}_i^{(j)} \cong \mathbf{H}_{x_i}^{(j)} \delta \mathbf{x}_{I,k} + \mathbf{H}_{f_j}^{(j)} \delta \hat{\mathbf{p}}_j^e + \mathbf{n}_i^{(j)} \tag{17}$$

where  $\mathbf{H}_{x_i}^{(j)}$  and  $\mathbf{H}_{f_j}^{(j)}$  are the Jacobians of  $\delta \mathbf{z}_i^{(j)}$  for  $\delta \mathbf{x}_{I,k}$  and  $\hat{\mathbf{p}}_j^e$ , respectively;  $\delta \hat{\mathbf{p}}_j^e$  is the error of  $\hat{\mathbf{p}}_j^e$ .

Generally, a static feature point is observed by multiple consecutive image frames; therefore, the measurement innovation of  $f_j$  in the sliding window can be expressed as follows:

$$\underbrace{\begin{bmatrix} \delta \mathbf{z}_1^{(j)} \\ \vdots \\ \delta \mathbf{z}_k^{(j)} \end{bmatrix}}_{\delta \mathbf{z}^{(j)}} \approx \underbrace{\begin{bmatrix} \mathbf{H}_{x_i}^{(j)} \\ \vdots \\ \mathbf{H}_{x_k}^{(j)} \end{bmatrix}}_{\mathbf{H}_f^{(j)}} \delta \mathbf{x}_{I,k} + \underbrace{\begin{bmatrix} \mathbf{H}_{f1}^{(j)} \\ \vdots \\ \mathbf{H}_{fk}^{(j)} \end{bmatrix}}_{\mathbf{H}_f^{(j)}} \delta \hat{\mathbf{p}}_j^e + \mathbf{n}^{(j)} \tag{18}$$

To convert  $\delta \mathbf{z}^{(j)}$  into an equation, which is related only to  $\delta \mathbf{x}_{I,k}$ , both sides of the equation are simultaneously

multiplied left by the left zero space matrix  $\mathbf{A}^T$  of  $\mathbf{H}_f^{(j)}$ .  $\delta \mathbf{z}^{(j)}$  can be rewritten as follows:

$$\begin{aligned} \delta \mathbf{z}_o^{(j)} &= \mathbf{A}^T (\mathbf{z}^{(j)} - \hat{\mathbf{z}}^{(j)}) \\ &= \mathbf{A}^T \mathbf{H}_x^{(j)} \delta \mathbf{x}_{I,k} + \mathbf{A}^T \mathbf{n}^{(j)} \\ &= \mathbf{H}_o^{(j)} \delta \mathbf{x}_{I,k} + \mathbf{n}_o^{(j)} \end{aligned} \tag{19}$$

Then, the measurement equations for all feature points are expressed as follows:

$$\mathbf{r}_{\text{Cl},k} = \mathbf{H}_{C,k} \delta \mathbf{x}_{I,k} + \mathbf{n}_{C,k} \tag{20}$$

where the measurement noise vector  $\mathbf{n}_{C,k}$  is modeled as a zero-mean GWN with covariance matrix  $\mathbf{R}_{C,k}$ . The detailed derivation of the equations for the visual measurement model can be found in Mourikis and Roumeliotis (2007).

For the tightly coupled GNSS/INS/Vision integration based on the EKF model, the state update equation at  $k$  epoch, as GNSS or visual measurements arrive, can be written as follows:

$$\hat{\mathbf{X}}_k = \hat{\mathbf{X}}_{k/k-1} + \mathbf{K}_k \mathbf{r}_k \tag{21}$$

where  $\mathbf{K}_k$  is the gain matrix,  $\hat{\mathbf{X}}_{k/k-1}$  and  $\hat{\mathbf{X}}_k$  are the predicted and optimized state vector, respectively, and  $\mathbf{r}_k$  is the innovation vector of the EKF. For example, as GNSS measurements are updated,  $\mathbf{r}_k$  can be marked as

$$\mathbf{r}_{\text{GL},k} = \begin{bmatrix} \mathbf{r}_{\rho I,k} \\ \mathbf{r}_{\rho I,k} \end{bmatrix} = \begin{bmatrix} \rho_I - \rho_G \\ \dot{\rho}_I - \dot{\rho}_G \end{bmatrix}, \text{ which is only associated with the GNSS measurement vector. Besides, it plays an important role in FDE.}$$

### Error and fault source of the system

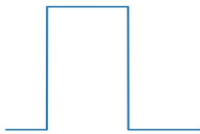
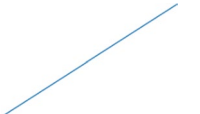



In previous research, the concepts of error and fault are usually confused, so a distinction is dictated here.

- *Error* This typically pertains to the difference between the sensor measurements and their corresponding true values.
- *Fault* Various sources of error that cause a navigation system to not work properly or it cannot provide accurate navigation solutions (unreliable navigation solutions).

The positioning accuracy of the system is strongly affected by fault sources, especially for multi-sensor integrated navigation systems, which increases the probability of system faults. Table 1 first summarizes the common error types and sources in GNSS/INS/Vision integration and subsequently analyzes the possible fault sources.

Constant bias and IMU bias can effectively be mitigated and estimated through sensor calibration and modeling, resulting in minimal impact on the navigation solutions once

**Table 1** Errors in the tightly coupled GNSS/INS/Vision integration (Jing et al. 2022)

Types	Shapes	Causes
Step error		Satellite clock jumps, severe vibration, abnormal temperature in the IMU, light changes, moving objects in the camera, etc.
SGEs		Satellite clock drifts, accumulation of errors in INS and visual navigation system, etc.
Constant Bias		IMU is not properly calibrated, inconsistent coordinate conversion, etc.
White noise		GNSS measurement noise, visual measurement noise, and IMU measurement noise
Random walk noise		Integration of white noise

corrected. Consequently, they are not classified as system faults. In contrast, step errors are more prevalent within this system and exert a significant influence on its positioning performance, while SGEs are challenging to detect and can lead to the unavailability of navigation solutions. Consequently, they are treated as faults.

As indicated by Eq. (21), the innovation vector of the EKF directly affects the accuracy of the filter states, even when it is affected by faults. Hence, the development of a fault detection and exclusion scheme is imperative. To illustrate this, taking the GNSS measurement vector as an example, and after compensating for receiver clock bias and drift correction,  $r_{GI,k}$  is redefined as follows in case of GNSS faults and IMU faults:

$$r_{GI,k} = G_{N_{sat} \times 3}^p \cdot (\epsilon_I + b_I) - \epsilon_G - b_G \tag{22}$$

where  $b_G$  and  $\epsilon_G$  indicate the GNSS fault vector and noise vector, respectively;  $\epsilon_I$  denotes the noise vector of the INS-derived navigation solution; and  $b_I$  is regarded as the bias vector of INS-derived navigation solutions impacted by IMU faults.

### Fault detection and exclusion scheme

First, the principles of AIME are described. Following this, we introduce an enhanced AIME method, referred to as PS-AIME. Subsequently, the two-step FD method is employed

to identify the source of the fault. Finally, the fault exclusion strategy is presented to ensure positioning performance in case of system faults.

### An enhanced AIME algorithm

AIME, being a typical fault detection method, exhibits superior performance in detecting SGEs in tightly coupled GNSS/INS integration (Bhatti et al. 2007). The test statistic of the AIME is computed as follows:

$$T_{s,k} = r_{avg}^T \cdot V_{avg}^{-1} \cdot r_{avg} \tag{23}$$

$V_{avg}$  and  $r_{avg}$  is given by:

$$\begin{cases} V_{avg}^{-1} = \sum_{i=k-l+1}^k V_{GI,i}^{-1} \\ r_{avg} = \left( V_{avg}^{-1} \right)^{-1} \sum_{i=k-l+1}^k V_{GI,i}^{-1} r_{GI,i} \end{cases} \tag{24}$$

where  $T_{s,k}$  follows a chi-square distribution and has the same freedom (DOF) as the number of visible satellites  $N_{sat}$ ;  $l$  is the length of the sliding window; and  $V_{GI,k}$  is the covariance matrix of the innovation vector  $r_{GI,k}$ , which can be calculated by:

$$V_{GI,k} = H_{GI,k} P_k^- H_{GI,k}^T + R_{GI,k} \tag{25}$$

where  $\mathbf{P}_k^-$  is the covariance matrix of the predicted state vector at epoch  $k$ . When  $T_{s,k}$  is greater than the test threshold  $T_{d,k}$ , the measurements are usually considered to be faulty.  $T_{d,k}$  is determined based on the probability of a false alarm  $P_{FA}$  and  $N_{\text{state}}$ , and it can be calculated by Jing et al. (2022):

$$1 - P_{FA} = F(T_{d,k} N_{\text{sat}}) \tag{26}$$

where  $F(*)$  is the cumulative distribution function of the central chi-squared distribution.

To identify faulty satellites, we introduce an improved AIME algorithm named PS-AIME. Once the innovation vector  $\mathbf{r}_{GL,k}$  and its covariance matrix  $\mathbf{V}_{GL,k}$  are computed, an innovation vector is categorized by satellite number and extended throughout the sliding window. Figure 2 provides a visual representation of this process.

As shown in Fig. 2,  $\mathbf{r}_{GL,ki}$  ( $i = 1, 2 \dots l$ ) indicates the innovation vector of the EKF algorithm at epoch  $ki$  in the sliding window, and  $\mathbf{S}_{GL,ki}^v$  is composed of the principal diagonal elements of the covariance matrix  $\mathbf{V}_{GL,ki}$  of  $\mathbf{r}_{GL,ki}$ . Here,  $\mathbf{S}_{ki}^{S_j}$  ( $j = 1, 2, \dots, N_{\text{sat}}$ ) can be considered as the covariance of  $r_{ki}^{S_j}$ .  $\mathbf{r}_{s_j}$  is composed up of the elements of the innovation vector associated with the satellite  $S_j$  at different moments in the sliding window. Then, inspired by the AIME algorithm, we calculated the test statistics for all visible satellites to enhance the detection ability of SGEs and identify faulty satellites. Taking satellite  $S_1$  as an example, its test statistic can be expressed as follows:

$$T_{S_1} = \mathbf{r}_{\text{avg},S_1}^T \cdot \mathbf{V}_{\text{avg},S_1}^{-1} \cdot \mathbf{r}_{\text{avg},S_1} \tag{27}$$

$\mathbf{V}_{\text{avg},S_1}$  and  $\mathbf{r}_{\text{avg},S_1}$  are obtained as follows:

$$\begin{cases} V_{\text{avg},S_1}^{-1} = \sum_{i=k-l+1}^k S_{ki}^{S_1-1} \\ r_{\text{avg},S_1} = \left( V_{\text{avg},S_1}^{-1} \right)^{-1} \sum_{i=k-l+1}^k S_{ki}^{S_1-1} r_{ki}^{S_1} \end{cases} \tag{28}$$

Notably, the test threshold  $T_{d,S_1}$  of  $T_{S_1}$  is derived from the probability of a false alarm  $P_{FA}$  and the length of the sliding window  $l$ .

### Separation of the GNSS, IMU, and visual fault

The AIME was designed to detect SGEs in GNSS measurements; however, determining the source of the fault is difficult in the case of (22). The primary objective is to distinguish and subsequently exclude sensor faults. Figure 3 visually depicts the various sensor fault scenarios within the state estimation process. Faults can originate from three sources: a satellite, an IMU, and a feature point. These faults directly impact GNSS and visual measurement models. The method for separating these faults is outlined as follows.

For the GNSS measurement model, first, test statistics affected only by GNSS faults are constructed. According to (22), the corresponding innovation-based vector can be formulated as follows:

$$\begin{aligned} \mathbf{r}_{G,k} &= \left( \mathbf{I}_{N_{\text{sat}} \times N_{\text{sat}}} - \mathbf{G}_{N_{\text{sat}} \times 3}^p \cdot \mathbf{A} \right) \cdot \mathbf{r}_{GL,k} \\ &= \left( \mathbf{G}_{N_{\text{sat}} \times 3}^p \cdot \mathbf{A} - \mathbf{I}_{N_{\text{sat}} \times N_{\text{sat}}} \right) \cdot \left( \boldsymbol{\varepsilon}_G + \mathbf{b}_G \right) \end{aligned} \tag{29}$$

where  $\mathbf{I}_{N_{\text{sat}} \times N_{\text{sat}}}$  denotes the identity matrix with  $N_{\text{sat}}$  rows and  $N_{\text{sat}}$  columns and  $\mathbf{A}$  are expressed as:

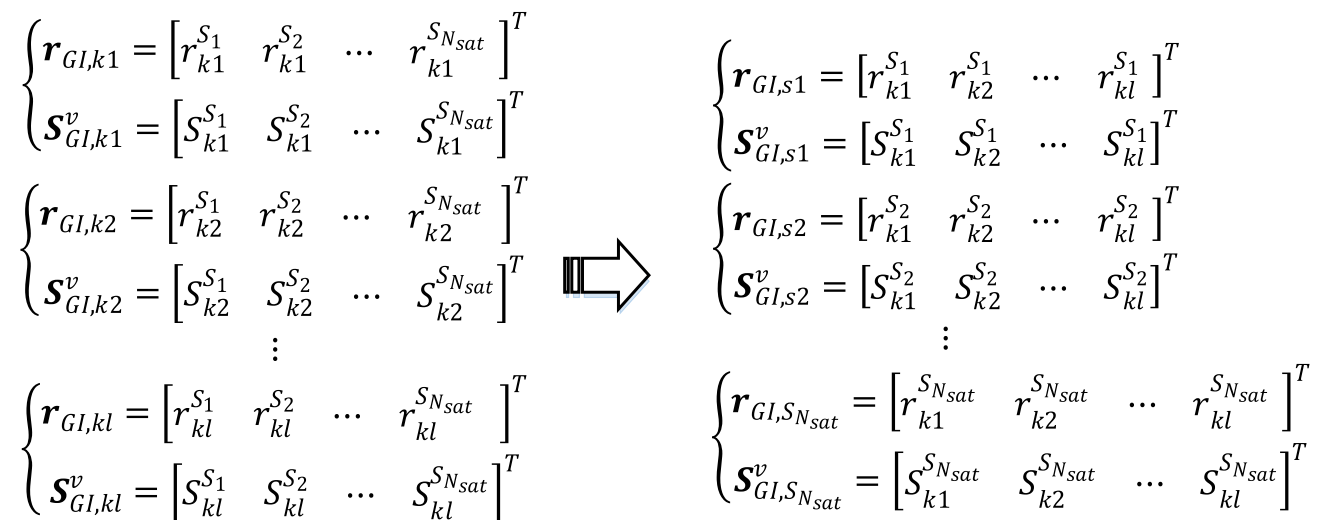


Fig. 2 Flowchart of the innovation vector grouped by satellite number in the sliding window

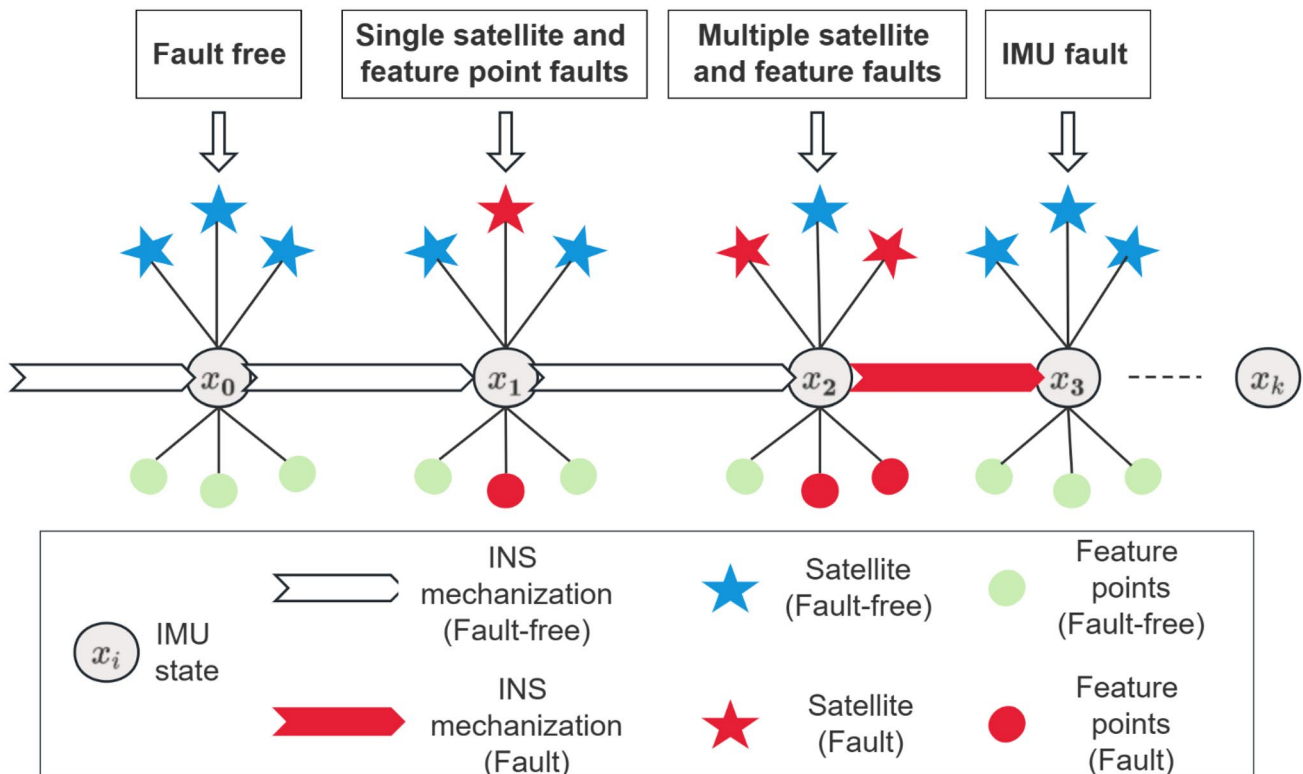


Fig. 3 Illustration of the state estimation process for different sensor fault situations

$$A = \left( \mathbf{G}_{N_{\text{sat}} \times 3}^{\rho T} \mathbf{G}_{N_{\text{sat}} \times 3}^{\rho} \right)^{-1} \cdot \mathbf{G}_{N_{\text{sat}} \times 3}^{\rho T} \quad (30)$$

Then, the covariance matrix of  $\mathbf{r}_{G,k}$  is written as:

$$\mathbf{V}_{G,k} = \left( \mathbf{G}_{N_{\text{sat}} \times 3}^{\rho} \mathbf{A} - \mathbf{I}_{N_{\text{sat}} \times N_{\text{sat}}} \right) \cdot \mathbf{V}_{\text{GL},k} \cdot \left( \mathbf{G}_{N_{\text{sat}} \times 3}^{\rho} \mathbf{A} - \mathbf{I}_{N_{\text{sat}} \times N_{\text{sat}}} \right)^T \quad (31)$$

As PS-AIME method in (27), the test statistic for each satellite can be calculated by  $\mathbf{r}_{G,k}$  and  $\mathbf{V}_{G,k}$  in the same way. Secondly, the test statistic  $T_{I,k}$  impacted by IMU faults is built as follows. The innovation-based vector is expressed as follows:

$$\hat{\mathbf{r}}_{I,k} = \mathbf{A} \cdot \mathbf{r}_{\text{GL},k} = \boldsymbol{\varepsilon}_I + \mathbf{b}_I - \mathbf{A} \cdot (\boldsymbol{\varepsilon}_G + \mathbf{b}_G) \quad (32)$$

As shown in (32),  $\hat{\mathbf{r}}_{I,k}$  cannot be directly used to calculate the test statistic  $T_{I,k}$  because GNSS faults also occur. These faults are handled by excluding GNSS faults and reducing their impact on vectors  $\hat{\mathbf{r}}_{I,k}$ . Similarly, the covariance matrix of  $\mathbf{r}_{I,k}$  is given as follows:

$$\mathbf{V}_{I,k} = \mathbf{A} \cdot \mathbf{V}_{\text{GL},k} \cdot \mathbf{A}^T \quad (33)$$

Then, the test statistic  $T_{I,k}$  is compared with the corresponding detection thresholds  $T_{dI,k}$  to assess whether an IMU fault has developed.

In the case of the visual measurement model, the influence of minor visual faults on navigation performance is considered negligible. Furthermore, when dealing with a substantial number of feature points, employing the AIME method for visual fault detection not only requires a higher detection threshold but also imposes a substantial computational load. To tackle these issues, a detection strategy for visual faults is developed. The specific steps are outlined as follows.

*Step1* Calculating the corresponding innovation  $\mathbf{r}_{\text{CI},k}$  and its variance matrix  $\mathbf{V}_{\text{CI},k}$ .

$$\mathbf{V}_{\text{CI},k} = \mathbf{H}_{C,k} \mathbf{P}_k^- \mathbf{H}_{C,k}^T + \mathbf{R}_{C,k} \quad (34)$$

*Step2* Calculating the normalized value of the  $j$ -th element of  $\mathbf{r}_{\text{CI},k}$ .

$$r_{Cj} = \frac{r_{\text{CI},kj}}{\sigma_{\text{V}_{\text{CI},k}}^j} \quad (35)$$

where  $r_{\text{CI},kj}$  denotes the  $j$ -th element of  $\mathbf{r}_{\text{CI},k}$ , and  $\sigma_{\text{V}_{\text{CI},k}}^j$  indicates the normalized variance of  $r_{\text{CI},kj}$ , which is  $T_{d,Cj}$  calculated by  $\mathbf{V}_{\text{CI},k}$ . If there is no visual fault,



**Fig. 4** Flowchart of the fault detection and exclusion strategy based on the innovation and covariance matrix of extended Kalman filtering

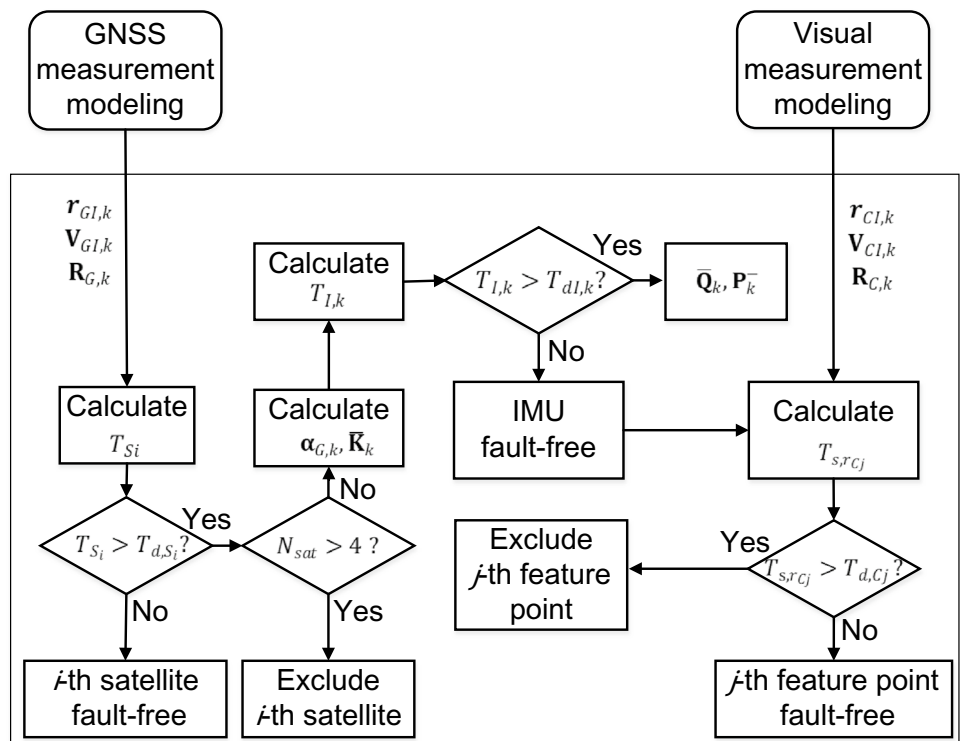


**Fig. 5** Experimental vehicle and equipment for data collection

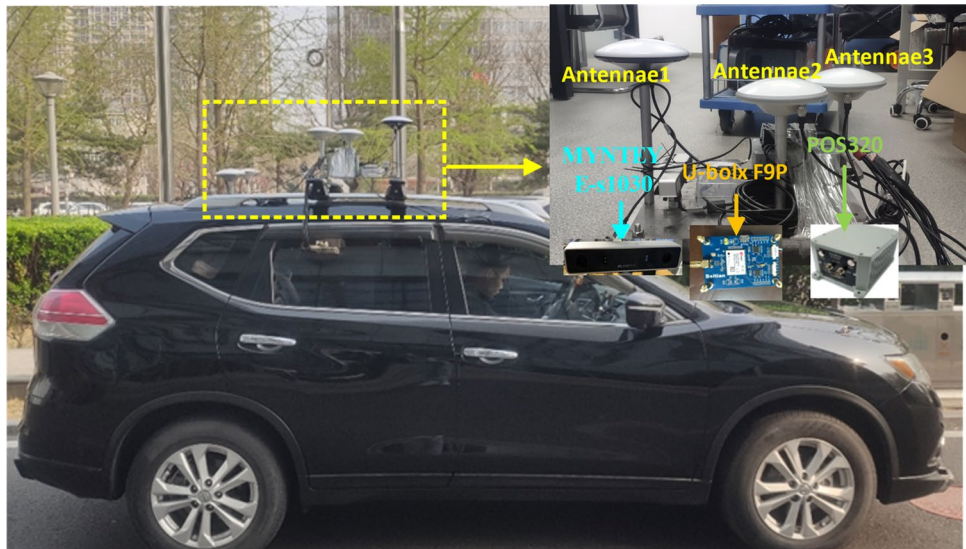


**Table 2** Key IMU parameters of the MYNTEYE-s1030 and POS320 equipment

IMU sensors	Parameters	MYNTEYE-s1030	POS320
Gyro	Bias (°/h)	845	0.5
	Noise (°/sqrt(h))	0.4	0.05
Accel	Bias (mg)	8450	25
	Noise (m/s/sqrt(h))	0.4	0.1

$$r_{Cj} \sim N(0, 1) \tag{36}$$

Step3 Calculating the test statistic of  $r_i$ .

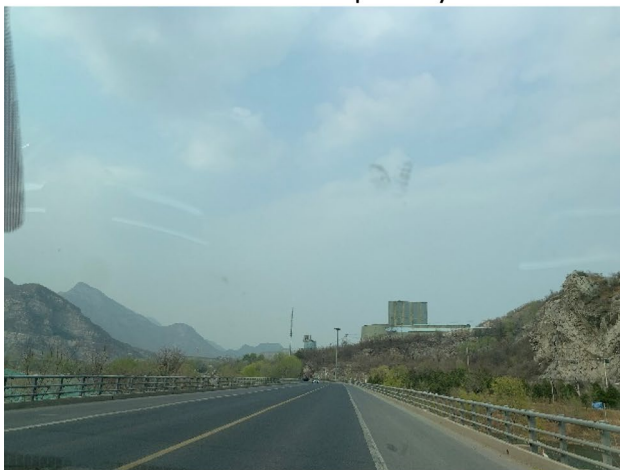
$$T_{s,rCj} = r_{Cj} \cdot r_{Cj} \tag{37}$$

Here,  $T_{s,rCj}$  can be considered as following a chi-square distribution with a degree of freedom 1. When  $T_{s,rCj}$  is greater than its corresponding detection threshold, the feature point



Fig. 6 Trajectory of the experimental vehicle in the test

Test case 1: Open sky



Test case 2: Slight signal blocking



Fig. 7 Environment of the field test case

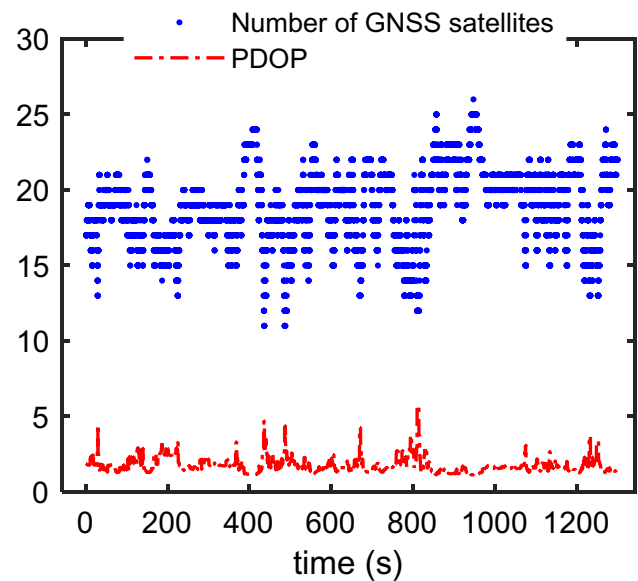


Fig. 8 Number of satellites and the corresponding position dilution of precision (PDOP) in the field test

measurement is deemed faulty in the absence of an IMU fault. Note that the probability of a false alarm  $P_{FA}$  is set to  $10^{-5}$ , which aligns with the standards in civil aviation fields. Moreover, 30%, 20%, and 50% of  $P_{FA}$  is allocated to IMU, GNSS, and visual fault detectors, respectively, under the principle that a high probability of a false alarm should be high if the prior probability of the sensor is large (Wang et al. 2020).

Fault exclusion strategy

The purpose of fault exclusion is to ensure the continuity of the system and the accuracy of the navigation solutions. There are different fault exclusion functions for satellites, IMU, and visual measurements due to their characteristics. For satellite measurements, when the number of visible satellites exceeds 4, the detected faulty satellites are excluded from consideration. However, if the number of visible satellites is 4 or fewer, the corresponding innovation is weighted. This approach is employed to eliminate faulty satellites while preserving the global positioning performance of the system to the greatest extent possible. The weight matrix  $\alpha_{G,k}$  is calculated by:

$$\alpha_{G,ki} = \begin{cases} 1, & T_{s,r_{Gi}} \leq T_{d,Gi} \\ \frac{T_{s,r_{Gi}}}{T_{d,Gi}}, & T_{s,r_{Gi}} > T_{d,Gi} \end{cases} \quad (38)$$

where  $\alpha_{G,ki}$  denotes the element of row  $i$  and column  $i$  of  $\alpha_{G,k}$ ;  $T_{s,r_{Gi}}$  indicates the test statistic of the  $i$ -th element in  $r_{GI,k}$ , which can be calculated by  $r_{GI,k}$  and  $V_{GI,k}$  in the same way as  $T_{r_{Ci}}$  (34–37); and  $T_{d,Gi}$  is the corresponding detection threshold.

**Table 3** Different fault situations

Case	Fault source (fault time)	Fault information
1	GNSS (500–620 s)	SGEs of magnitude 0.1 m/s to SV-133
2		SGEs of magnitude 0.1 m/s to SV-1 and SV-127
3	IMU (500–510 s)	0.005 rad/s and 0.05 m/s <sup>2</sup> step faults to each gyroscope and accelerometer axis, respectively
4		0.05 rad/s and 0.5 m/s <sup>2</sup> step faults to each gyroscope and accelerometer axis, respectively
5		0.5 rad/s and 1 m/s <sup>2</sup> step faults to each gyroscope and accelerometer axis, respectively

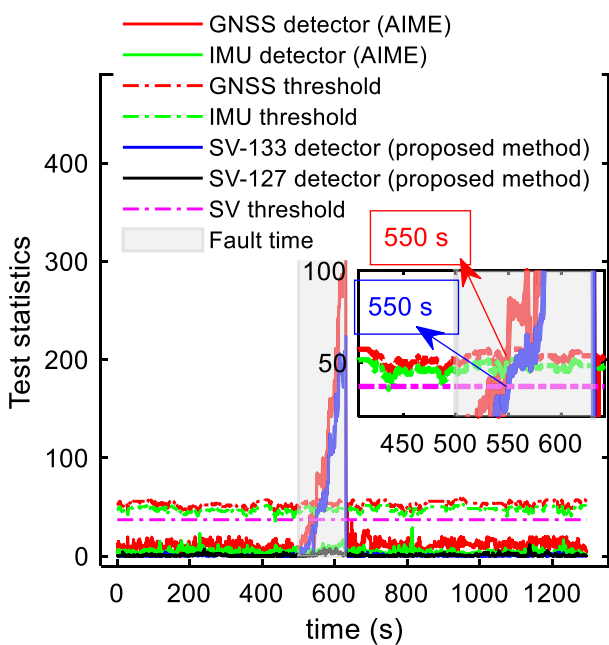


**Fig. 9** Test statistics for GNSS SGEs of magnitude 0.1 m/s occurring in single satellite pseudorange measurements

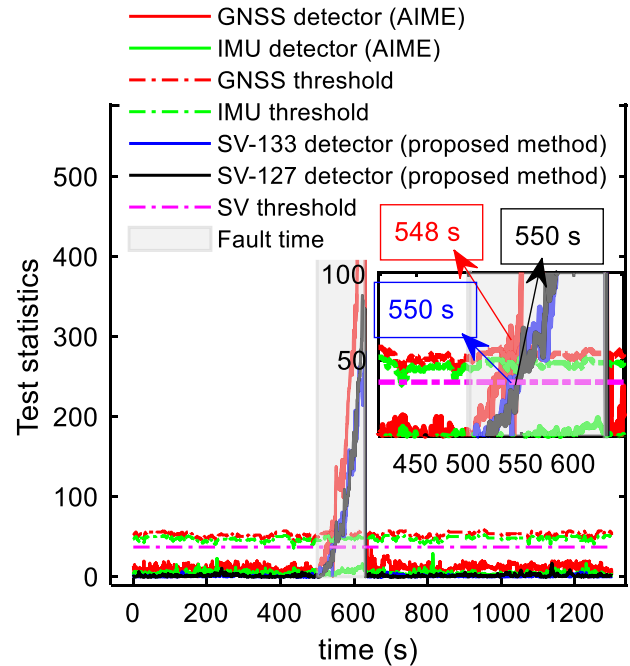


**Fig. 10** Test statistics for GNSS SGEs of magnitude 0.1 m/s occurring in two satellite pseudorange measurements

Then, the state update equation at  $k$  epoch, as GNSS measurements arrive, can be rewritten as follows:

$$\begin{cases} \bar{\mathbf{R}}_{G,k} = \boldsymbol{\alpha}_{G,k} * \mathbf{R}_{G,k} \\ \bar{\mathbf{K}}_k = \mathbf{P}_k^- \mathbf{H}_{G,k}^T (\mathbf{H}_{G,k} \mathbf{P}_k^- \mathbf{H}_{G,k}^T + \bar{\mathbf{R}}_{G,k})^{-1} \\ \hat{\mathbf{X}}_k = \hat{\mathbf{X}}_{k/k-1} + \bar{\mathbf{K}}_k \cdot \mathbf{r}_{GL,k} \end{cases} \quad (39)$$

The IMU faults seriously deteriorate the navigation performance of the system because it is tightly fused with both the GNSS and visual measurements. In this section, once the IMU faults are detected, the system noise matrix  $\mathbf{Q}_k$  is recalculated to ensure the accuracy of the navigation solutions.

$$\begin{cases} \bar{\mathbf{Q}}_k = \beta_k \cdot \mathbf{Q}_k \\ \mathbf{P}_k^- = \boldsymbol{\Phi}_{k/k-1} \mathbf{P}_{k-1}^+ \boldsymbol{\Phi}_{k/k-1}^T + \bar{\mathbf{Q}}_k \end{cases} \quad (40)$$

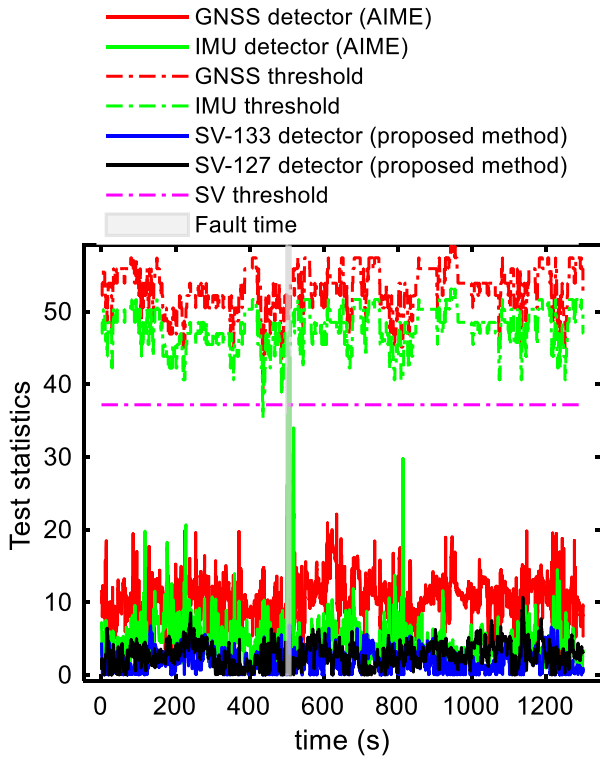
$$\beta_k = \begin{cases} 1, & T_{I,k} \leq T_{dl,k} \\ T_{I,k}, & T_{I,k} > T_{dl,k} \end{cases} \quad (41)$$

where  $\boldsymbol{\Phi}_{k/k-1}$  denotes the state transition matrix of the EKF;  $\mathbf{P}_{k-1}^+$  denotes the corrected covariance matrix of the EKF at epoch  $k - 1$ .

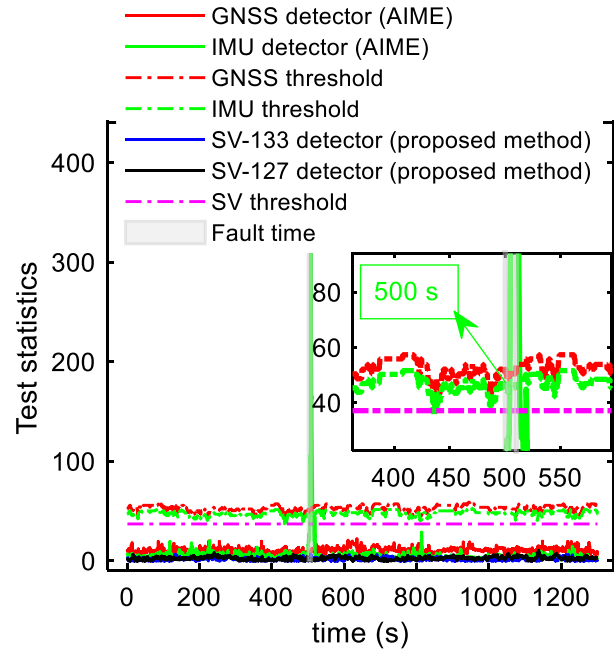
For visual measurements, faulty measurements are directly excluded owing to the large number of feature points in an outdoor environment. Figure 4 provides an illustrative flowchart of the FDE strategy, which relies on the innovation and covariance matrix of the EKF.

As shown in Fig. 4, the FDE strategy first separates GNSS and IMU faults using the GNSS measurement modeling and second detects IMU faults in the presence of detecting and excluding faulty satellites. Finally, visual measurement modeling is used to detect and exclude visual faults under the premise of excluding IMU faults.

Case 3 in Table 3: 0.005 rad/s (gyroscope) and 0.05 m/s<sup>2</sup> (accelerometer)



Case 4 in Table 3: 0.05 rad/s (gyroscope) and 0.5 m/s<sup>2</sup> (accelerometer)



Case 5 in Table 3: 0.5 rad/s (gyroscope) and 1 m/s<sup>2</sup> (accelerometer)

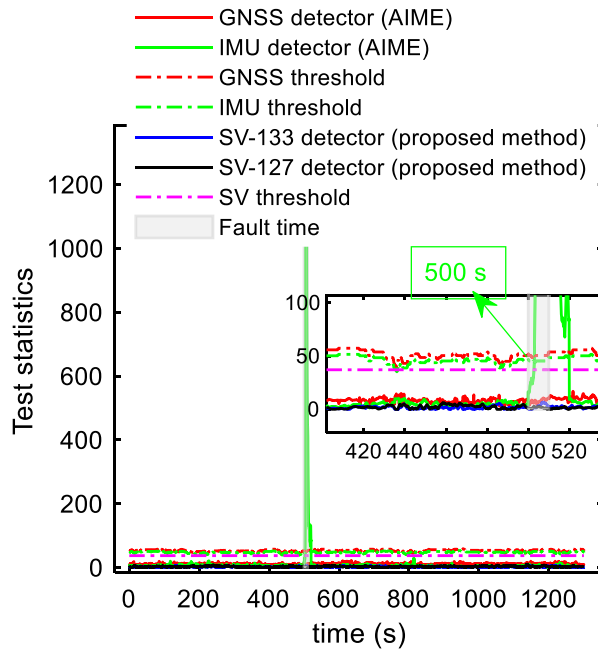
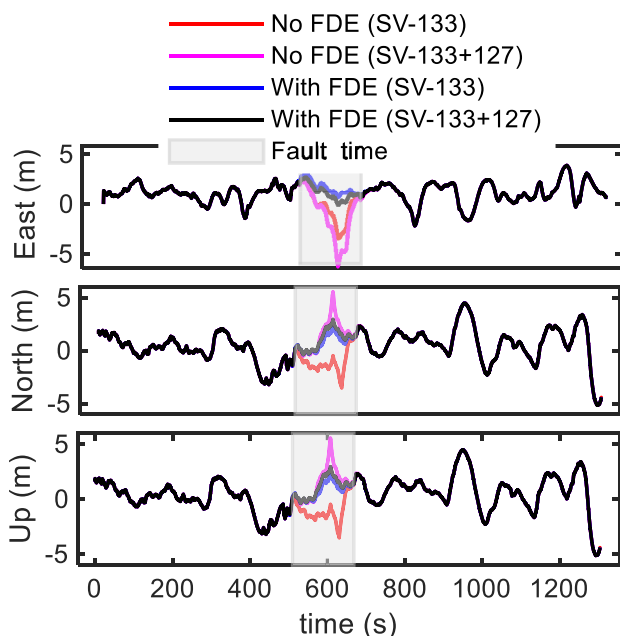


Fig. 11 Test statistics for step faults with different amplitudes occurring in IMU measurements



**Fig. 12** Positioning error in east, north, and up direction before and after fault detection and exclusion in the GNSS fault situation. FDE (fault detection and exclusion)

**Evaluation of field tests**

A field test was conducted to validate the proposed algorithm on April 1, 2023, in Beijing, China. Figure 5 provides an overview of the experimental vehicle and equipment utilized for data collection. The raw GNSS data were gathered using a u-blox F9P board at a sampling rate of 10 Hz, while the raw IMU data and images were collected using the MYNTEYE-s1030 module. It is important to note that the timestamp associated with the GNSS data is based on GPS time, whereas the timestamp associated with the IMU data and images is Coordinated Universal Time (UTC). Currently, there is an 18-s time difference between the two timestamps. The IMU timestamp and image timestamp are hardware-synchronized. The reference trajectory was determined by the postprocessing kinematic mode of NovAtel Inertial Explorer software with tactical-grade GNSS/INS POS320.

The POS320 navigator was linked to antenna 2, while the U-blox F9P board was connected to antenna 1. Key IMU parameters for both the MYNTEYE-s1030 and POS320 equipment are summarized in Table 2. Additionally, Fig. 6 provides a visual representation of the driving trajectory followed by the experimental vehicle during this test. The GNSS observation conditions along the test route are exhibited in Fig. 7.

Figure 8 shows the number of observed satellites and the corresponding position dilution of precision (PDOP) values.

The results show that the PDOP values in field tests are commonly low (in the test case 1 environment) and sometimes high (in the test case 2 environment). Overall, this approach is good for positioning.

**Verification of the fault detection capability**

To evaluate the fault detection capability of the proposed method, various faults were manually introduced into the satellite pseudorange and IMU raw measurements, as outlined in Table 3. Specifically, we focused on satellites 133 (SV-133) and 127 (SV-127). For pseudorange measurements, SGEs with a slope of 0.1 m/s were introduced as typical faults, while different magnitudes of step faults were applied to each gyroscope and accelerometer axis for IMU raw measurements. These step faults were selected based on the principle that they should be an order of magnitude less than, equal to, and greater than the current IMU raw data, as applicable.

Figures 9 and 10 depict the test statistics for AIME and the proposed PS-AIME method in the GNSS fault scenarios (Cases 1 and 2 in Table 3). The results show that while there is a slight difference in the fault detection time between the two methods, the proposed PS-AIME method is effective in identifying faulty satellites. Furthermore, the test statistic for the IMU consistently remains below its corresponding threshold in the GNSS fault situation, providing further evidence of the effectiveness of the GNSS fault exclusion approach.

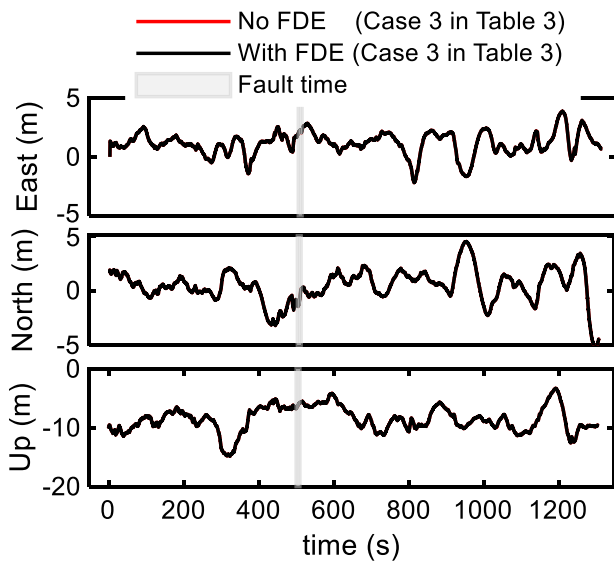
Figure 11 displays the test statistics for step faults with varying amplitudes in the IMU fault scenarios (Cases 3, 4, and 5 in Table 3). The findings reveal that significant step faults are promptly detected, whereas minor faults go undetected. This discrepancy arises from the fact that the EKF is capable of estimating and compensating for small IMU faults in real time, resulting in minimal impact on the residual vector in Eq. (32).

**Positioning performance before and after fault exclusion**

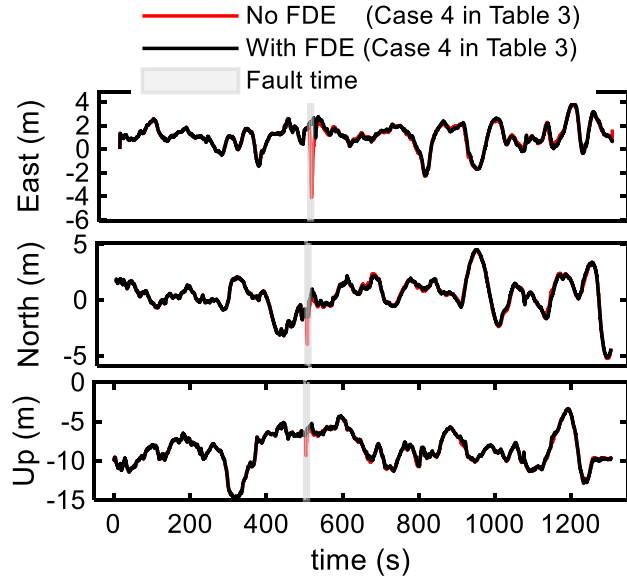
To provide further evidence of the fault exclusion strategy’s effectiveness, Fig. 12 contrasts the positioning errors in the east, north, and up (ENU) directions both before and after FDE in the GNSS fault situation. The outcomes demonstrate that the system’s position error during the fault occurrence is reduced from a maximum of – 6.2 to – 0.6 m after fault detection and exclusion. This results in a 90% reduction in positional error. The proposed FDE method is effective at detecting and excluding faulty satellites to ensure the positioning performance of the system.

Figure 13 shows the positioning errors in the ENU direction before and after FDE in the IMU fault situation. As depicted in this figure, the results indicate that in the case of

Case 3 in Table 3: 0.005 rad/s (gyroscope) and 0.05 m/s<sup>2</sup> (accelerometer)



Case 4 in Table 3: 0.05 rad/s (gyroscope) and 0.5 m/s<sup>2</sup> (accelerometer)



Case 5 in Table 3: 0.5 rad/s (gyroscope) and 1 m/s<sup>2</sup> (accelerometer)

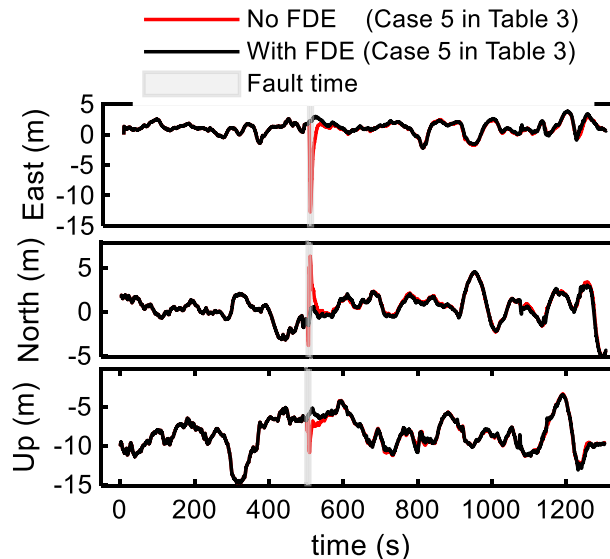


**Fig. 13** Positioning error in east, north, and up directions before and after fault detection and exclusion in the IMU fault situation

Case 3 from Table 3, although minor IMU faults go undetected, as shown in Fig. 10, they exert negligible influence on the system's positioning performance. Furthermore, for Cases 4 and 5 in Table 3, the positioning performance experiences a significant degradation before FDE, highlighting the effectiveness of the proposed fault exclusion method. The findings reveal that the system's position error during fault occurrence is reduced from a maximum of  $-13.8$  to

$1.3$  m before and after fault detection and exclusion. This represents a 91% reduction in positional error. Specifically, when an IMU fault is detected, its impact on the accuracy of the system state estimation can be mitigated by increasing the process matrix  $\mathbf{Q}_k$ .

Figures 14 and 15 provide information on the number of feature points and the positioning error in ENU direction before and after FDE in a real-world visual fault scenario.

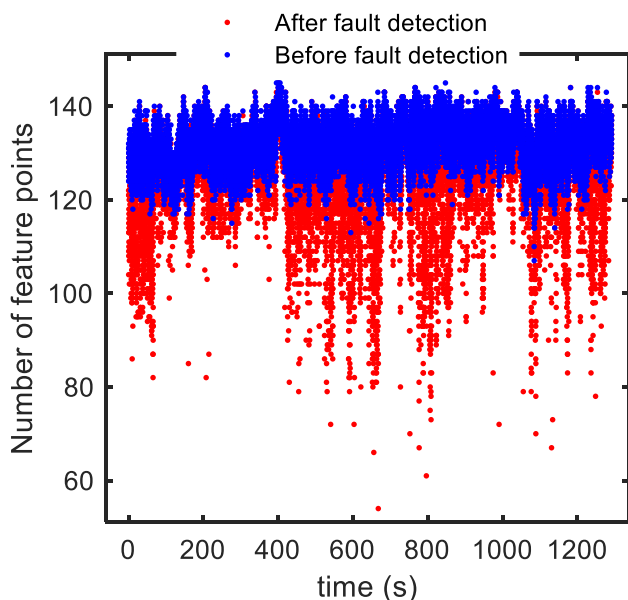


**Fig. 14** Number of feature points before and after fault detection and exclusion

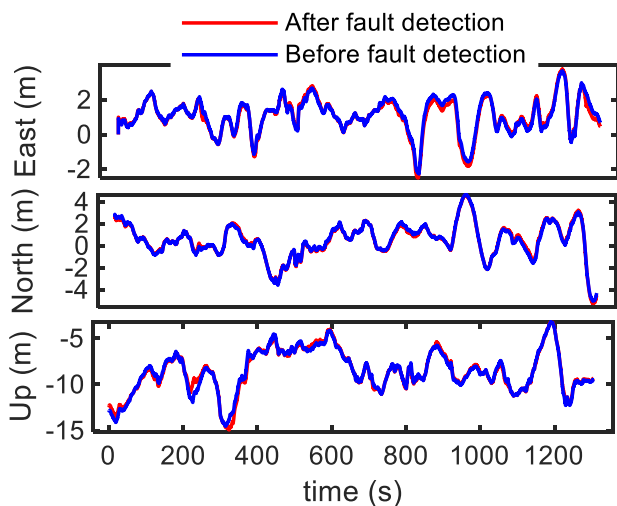


**Fig. 15** Positioning errors in east, north, and up directions before and after fault detection and exclusion in real-world visual fault situation

The results reveal a significant alteration in the number of feature points before and after FDE, but the improvement in the system’s positioning accuracy is relatively minor. This discrepancy arises from the fact that the global positioning accuracy of the system is primarily influenced by the performance of the GNSS. The contribution of the visual navigation system to positioning accuracy becomes more apparent when GNSS signals are heavily obstructed or unavailable.

To further assess the effectiveness of the proposed method, Table 4 compiles the maximum values of the

**Table 4** The maximum values of position error in east, north, and up directions before and after fault detection and exclusion (FDE) for different sensor faults

Fault source	Fault-NO FDE North/East/Up (m)	Fault-with FDE North/East/Up (m)
Case 1 in Table 3	-3.8/-3.9/-3.7	0.2/1.5/1.4
Case 2 in Table 3	-6.1/5.7/5.8	-0.6/2.1/2.2
Case 3 in Table 3	2.3/-1.2/-6.8	2.3/-1.2/-6.8
Case 4 in Table 3	-4.1/-3.9/-9.5	2.4/-1.3/-6.9
Case 5 in Table 3	-14.1/7.2/-11.3	2.3/-1.5/-7.1

system’s position error in ENU directions before and after FDE for various sensor faults. The results demonstrate that, in comparison with the pre-FDE state, the maximum system position error at the time of fault is reduced by an average of 72% and 56% in the scenarios involving GNSS fault modes and IMU fault modes, respectively.

To further illustrate the performance of visual navigation, Fig. 16 displays the positioning errors in the ENU directions for GNSS/INS integration and GNSS/INS/Vision integration when the GNSS signal was completely obstructed from 20 to 70 s. As depicted in the figure, the maximum position errors for GNSS/INS integration and GNSS/INS/Vision integration were -495 m and -21 m, respectively, when satellite signals were blocked. The system’s position error was reduced by 96% with the assistance of visual navigation. This approach significantly enhances the system’s positioning performance and robustness. This improvement stems from the fact that GNSS/INS integration relies solely on IMU mechanization and is not constrained by environmental factors.

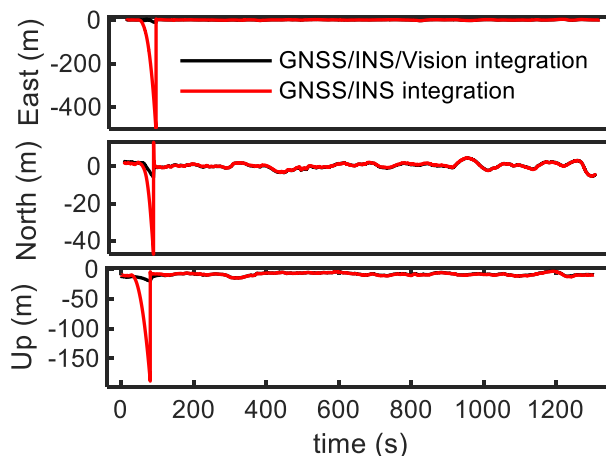


**Fig. 16** Positioning error in east, north, and up direction of two integrated navigation systems when the GNSS signal is completely blocked

## Conclusions

We introduce an innovation-based Kalman filter fault detection and exclusion method tailored for addressing all-source faults within tightly coupled GNSS/INS/Vision integration. Theoretical analyses are conducted to evaluate the impact of sensor faults on the system's state estimation. We employ a two-step fault separation approach to accurately detect and distinguish between GNSS faults and IMU faults. Additionally, we propose an enhanced AIME method named PS-AIME, which effectively identifies faulty satellites and promptly removes them from the system. Furthermore, we design straightforward yet validated fault exclusion strategies to mitigate the influence of various sensor faults on the system's positioning performance. Field tests are conducted in a vehicle mobility navigation application to validate the efficacy of our approach. The experimental outcomes demonstrate that (a) the two-step fault separation method effectively distinguishes GNSS and IMU faults, (b) the proposed PS-AIME method rapidly detects faulty satellites, (c) our proposed FDE method effectively safeguards GNSS/INS/Vision integration against all-source faults, and (d) visual feature point measurement faults in real-world environments have limited impact on the system's positioning accuracy. Future work will concentrate on implementing the visual-assisted fault detection technique in scenarios where satellite signals are heavily obstructed.

**Acknowledgements** Not applicable

**Author contributions** HJ and DY were involved in conceptualization and methodology; HJ was involved in data acquisition, experiment, and writing—original draft; JW was involved in formal analysis; DY, JW, and JY were involved in supervision; and HJ, DY, JW, and JY were involved in writing—review and editing. All authors have read and agreed to the published version of the manuscript.

**Funding** This work was supported by the Science and Technology Project of State Grid Corporation of China (Research and Application of Key Technologies for Autonomous and Controllable Power Beidou High Reliable Space-Time Service, No. 5700-202441237A-1-1-ZN).

**Data availability** The datasets analyzed during the current study are available from the corresponding author.

## Declarations

**Conflict of interest** There are no financial conflicts of interest to disclose.

**Ethical approval** Not applicable.

**Consent to participate** Not applicable.

**Consent for publication** We kindly consent for the publication of identifiable information and materials related to the participants involved in this study.

## References

- Backén S, Akos D, Chu T, Guo N (2012) Monocular camera/IMU/GNSS integration for ground vehicle navigation in challenging GNSS environments. *Sensors* 12(3):3162–3185. <https://doi.org/10.3390/s120303162>
- Bhatti UI, Ochieng WY, Feng S (2007) Integrity of an integrated GPS/INS system in the presence of slowly growing errors part I: a critical review. *GPS Solut* 11(3):173–181. <https://doi.org/10.1007/s10291-006-0048-2>
- Bhatti UI, Ochieng WY, Feng S (2012) Performance of rate detector algorithms for an integrated GPS/INS system in the presence of slowly growing error. *GPS Solut* 16:293–301. <https://doi.org/10.1007/s10291-011-0231-y>
- Blanch J, Ene A, Walter T, Enge P (2007) An optimized multiple hypothesis raim algorithm for vertical guidance. In: Proceedings of the 20th international technical meeting of the satellite division of the institute of navigation, pp 2924–2933.
- Blanch J, Walter T, Enge P (2018) A formula for solution separation without subset solutions for advanced RAIM. In: 2018 IEEE/ION position, location and navigation symposium (PLANS), pp 316–326.
- Brenner M (1996) Integrated GPS/inertial fault detection availability. *Navigation* 43(2):111–130. <https://doi.org/10.1002/j.2161-4296.1996.tb01920.x>
- Cao S, Lu X, Shen S (2021) GVINS: tightly coupled GNSS-visual-inertial for smooth and consistent state estimation. *IEEE Trans Robot* 38(4):2004–2021. <https://doi.org/10.48550/arXiv.2103.07899>
- Chen K, Chang G, Chen C (2021) GINav: a MATLAB-based software for the data processing and analysis of a GNSS/INS integrated navigation system. *GPS Solut* 25(3):1–7. <https://doi.org/10.1007/s10291-021-01144-9>
- Crispoltoni M, Fravolini M, Balzano F, D'Urso S, Napolitano M (2018) Interval fuzzy model for robust aircraft IMU sensors fault detection. *Sensors* 18(8):2488. <https://doi.org/10.3390/s18082488>
- Diesel J, Luu S (1995) GPS/IRS AIME: Calculation of thresholds and protection radius using chi-square methods. In: Proceedings of the 8th international technical meeting of the satellite division of the institute of navigation (ION GPS 1995), pp 1959–1964
- Groves P (2013) Principles of GNSS, inertial, and multisensor integrated navigation systems—second edition. *J Navig* 67(1):191–192
- Jing H, Gao Y, Shahbeigi S, Dianati M (2022) integrity monitoring of GNSS/INS based positioning systems for autonomous vehicles: state-of-the-art and open challenges. *IEEE Trans Intell Transp Syst* 23(9):14166–14187. <https://doi.org/10.1109/TITS.2022.3149373>
- Lee J, Kim M, Lee J, Pullen S (2018) Integrity assurance of Kalman-filter based GNSS/IMU integrated systems against IMU faults for UAV applications. In: Proceedings of the 31st international technical meeting of the satellite division of the institute of navigation (ION GNSS+ 2018), pp 2484–2500. <https://doi.org/10.33012/2018.15977>
- Li T, Zhang H, Gao Z, Niu X, El-Sheimy N (2019) Tight fusion of a monocular camera, MEMS-IMU, and single-frequency multi-GNSS RTK for precise navigation in GNSS-challenged environments. *Remote Sens* 11(6):610. <https://doi.org/10.3390/rs11060610>
- Liu W, Song D, Wang Z, Fang K (2019) Error overboundings of KF-based IMU/GNSS integrated system against IMU faults. *Sensors* 19(22):4912. <https://doi.org/10.3390/s19224912>
- Misra P, Enge P (2001) Global positioning system: signals, measurements, and performance. In: *IEEE aerospace and electronic*



systems magazine, vol 17, No (10), pp 36–37. <https://doi.org/10.1109/MAES.2002.1044515>

- Mourikis AI, Roumeliotis SI (2007) A multi-state constraint Kalman filter for vision-aided inertial navigation. In: Proceedings 2007 IEEE international conference on robotics and automation pp 3565–3572. <https://doi.org/10.1109/ROBOT.2007.364024>
- Ochieng WY, Feng S (2008) User level integrity monitoring and quality control for high accuracy positioning using GPS/INS measurements. *J Glob Position Syst* 7(2):104–114. <https://doi.org/10.5081/jgps.7.2.104>
- Pan W, Zhan X, Zhang X, Wang S (2019) A subset-reduced method for FDE ARAIM of tightly-coupled GNSS/INS. *Sensors* 19(22):4847. <https://doi.org/10.3390/s19224847>
- Pasquale GD, Somà A (2010) Reliability testing procedure for MEMS IMUs applied to vibrating environments. *Sensors* 10(1):456–474. <https://doi.org/10.3390/s100100456>
- Tanil C, Khanafseh S, Joerger M, Kujur B, Pervan B (2019) Optimal INS/GNSS coupling for autonomous car positioning integrity. In: Proceedings of the 32nd international technical meeting of the satellite division of the institute of navigation (ION GNSS+ 2019), pp 3123–3140. <https://doi.org/10.33012/2019.17013>
- Wang S, Zhan X, Zhai Y, Liu B (2020) Fault detection and exclusion for tightly coupled GNSS/INS system considering fault in state prediction. *Sensors*. <https://doi.org/10.3390/s20030590>
- Yang L, Li Y, Wu Y, Rizos C (2014) An enhanced MEMS-INS/GNSS integrated system with fault detection and exclusion capability for land vehicle navigation in urban areas. *GPS Solut* 18(4):593–603. <https://doi.org/10.1007/s10291-013-0357-1>
- Yin J, Li A, Li T, Yu W, Zou D (2021) M2DGR: A multi-sensor and multi-scenario SLAM dataset for ground robots. *IEEE Robot Autom Lett* 7(2):2266–2273. <https://doi.org/10.1109/LRA.2021.3138527>

**Publisher's Note** Springer Nature remains neutral with regard to jurisdictional claims in published maps and institutional affiliations.

Springer Nature or its licensor (e.g. a society or other partner) holds exclusive rights to this article under a publishing agreement with the author(s) or other rightsholder(s); author self-archiving of the accepted manuscript version of this article is solely governed by the terms of such publishing agreement and applicable law.



**Haitao Jiang** received an MS degree from Taiyuan University of Technology, Taiyuan, China, in 2019. He is currently working toward a PhD degree with the School of Electronics and Information Engineering, Beihang University. Her current research mainly involves multisource fusion navigation and integrity monitoring, which includes GNSS, inertial and visual integrated navigation.



**Dayu Yan** is currently pursuing a PhD degree at the School of Electronics and Information Engineering, Beihang University, Beijing, China. His current research interests include multi-source fusion for robots, pedestrian navigation, and indoor positioning, which includes GNSS, inertial, and visual integrated navigation.



**Jiale Wang** is currently a PhD candidate at the School of Electronic and Information Engineering, at Beihang University. He received his bachelor's degree in Communication and Information Systems from Beijing Jiaotong University in 2019. His current research focuses on high-precision GNSS positioning, multi-sensor fusion, and seamless indoor-outdoor navigation.



**Jie Yin** received a BS degree in electrical engineering from Shanghai Jiao Tong University, Shanghai, China, in 2021. And he is currently pursuing a master's degree at Shanghai Jiao Tong University, in Shanghai, China. His current research interests include computer vision, robotics, multi-sensor fusion, and simultaneous localization and mapping (SLAM).